

# Accuracy Performance of Star Trackers—A Tutorial

CARL CHRISTIAN LIEBE

Jet Propulsion Laboratory  
California Institute of Technology

An autonomous star tracker is an avionics instrument used to provide the absolute 3-axis attitude of a spacecraft utilizing star observations. It consists of an electronic camera and associated processing electronics. The processor has the capability to perform star identification utilizing an internal star catalog stored in firmware and to calculate the attitude quaternion autonomously. Relevant parameters and characteristics of an autonomous star tracker are discussed in detail.

Manuscript received March 5, 2001; revised January 7, 2002;  
released for publication January 28, 2002.

IEEE Log No. T-AES/38/2/11444.

Refereeing of this contribution was handled by J. T. Burnett.

The research described in this paper was carried out at the Jet Propulsion Laboratory, California Institute of Technology and was sponsored by the National Aeronautics and Space Administration. References herein to any specific commercial product, process or service by trademark, manufacturer, or otherwise, does not constitute or imply its endorsement by the United States Government or the Jet Propulsion Laboratory, California Institute of Technology.

Author's address: Jet Propulsion Laboratory, California Institute of Technology, MS 198-138, 4800 Oak Grove Dr., Pasadena, CA 91109-8099, E-mail: (carl.c.liebe@jpl.nasa.gov).

0018-9251/02/\$17.00 © 2002 IEEE

## I. INTRODUCTION

Star trackers have recently undergone a generation shift. First generation star trackers were characterized by acquiring a few bright stars and outputting the focal plane coordinates of these stars to the spacecraft computer. The coordinates were not related to inertial space and therefore no attitude information was provided directly. The star identification and the attitude determination had to be done externally to the star tracker. In the last decade, the availability of space qualified powerful microcomputers has allowed the star observations to be compared against a stored firmware star catalog. Thus the rotation from an inertial based coordinate system to a star tracker based coordinate system can be calculated directly [1].

Autonomous star trackers are rapidly becoming the preferred attitude determination instruments onboard most spacecraft. This is primarily due to simple integration of the self-contained autonomous unit and low cost compared with first generation star trackers or other instruments for attitude determination. The market volume over the next 10 years could be several hundred units. This has attracted many vendors to the market. An open literature/web search shows more than 15 star tracker vendors offering star trackers [2–16] at rapidly decreasing costs.

Basically, a star tracker is an electronic camera<sup>1</sup> connected to a microcomputer. Using a sensed image of the sky, stars can be located and identified. The orientation of the spacecraft can be determined based on these observations. An autonomous star tracker automatically performs pattern recognition of the star patterns in the field of view (FOV) and calculates the attitude with respect to the celestial sphere. Fig. 1 shows a sketch of a modern star tracker [23]. A typical (year 2001) autonomous star tracker has a mass of 1–7 kg and consumes 5–15 W of power. The accuracy is in the arcsecond range and update rates are typically 0.5–10 Hz [24]. It is anticipated that the ongoing technology development will decrease the power consumption and mass of autonomous star trackers significantly. However, since the number of photons from the stars is finite, no major improvements in the update rate or the accuracy is anticipated in the future.

The operation of a star tracker is described in this work. The performance of the star tracker depends on the sensitivity to starlight, FOV, the accuracy of the star centroiding, the star detection threshold, the number of stars in the FOV, the internal star catalog,

<sup>1</sup>Typically a Charge Coupled Device (CCD) focal plane array is used. However, Charge Injected Devices (CID) [17, 18] and Active Pixel Sensors (APS) [19, 20] have also been utilized. APS has the advantage of low power consumption and logic integrated on the focal plane itself (e.g. centroiding and A/D conversion [21, 22]). CIDs are inherently very radiation tolerant.

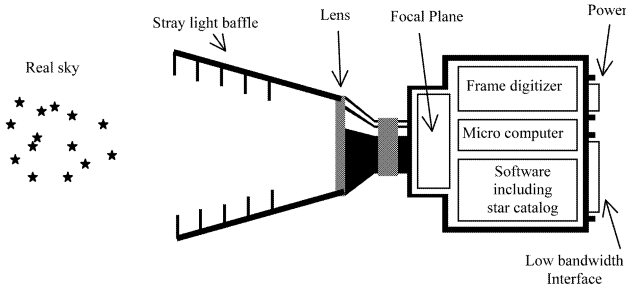


Fig. 1. Sketch of an autonomous star tracker.

and the calibration. These topics are discussed in detail. The accuracy of the star tracker is typically divided into different components such as line of sight stability, relative accuracy, calibration errors, noise equivalent angle (NEA), S-curve errors and algorithmic errors. These categories and measurements of the NEA and the relative accuracy utilizing a telescope drive are discussed.

## II. STAR TRACKER OPERATION

An autonomous star tracker typically operates in two modes: 1) initial attitude acquisition and 2) tracking mode. The difference between the modes is whether approximate attitude knowledge is available. In initial attitude acquisition, the task is to perform pattern recognition of the star pattern in the FOV. Many algorithms have been developed to perform this function [25–31]. Typically, the identification can be accomplished in a few seconds. Normal operating mode (tracking mode) assumes that the present attitude is close to the last attitude update ( $\sim$  less than 1 s ago). The task is much easier since the star tracker only has to track previously identified stars at known positions.

A typical star tracker image is shown in Fig. 2.<sup>2</sup> It is observed that the image is slightly defocused. This is to overcome the sampling theorem, which otherwise limits the accuracy to 0.38 pixel.<sup>3</sup> Different algorithms for calculating star centroids exist [23, 32, 33]. The calculated star centroids for this image is shown in Fig. 3. Centroiding is discussed further in Section IV.

Attitude and rate information from previous exposures is used in the tracking mode to predict star positions in the next exposure. Therefore, it is not necessary to digitize the entire image. Some star trackers utilize special hardware that only digitizes specific small windows in the image at predicted star positions. An example is shown in Fig. 4. This technique reduces the processor load significantly.

The positions of the star centroids on the focal plane can be transformed into unit vectors in a star

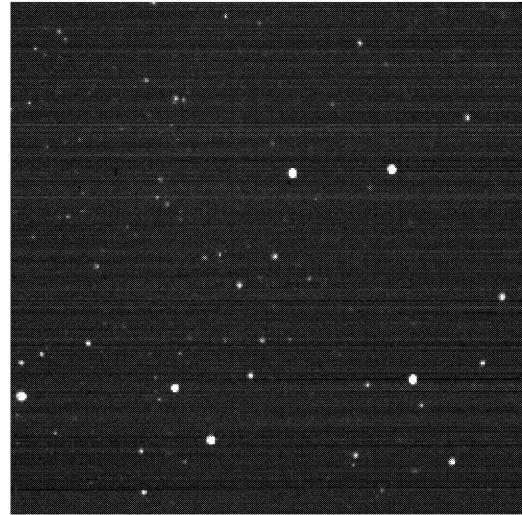


Fig. 2. Star tracker image.

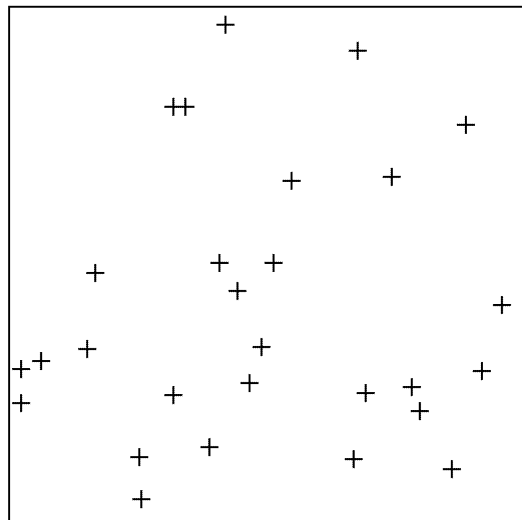


Fig. 3. The brightest centroids.

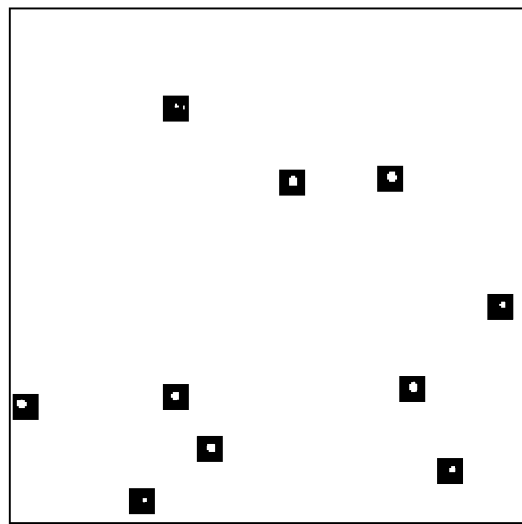


Fig. 4. The star image from Fig. 2. This Image is only digitized around predicted star positions.

<sup>2</sup>The image has been acquired by a JPL developmental APS based star tracker [19].

<sup>3</sup> $\int_{-0.5}^{0.5} \int_{-0.5}^{0.5} \sqrt{x^2 + y^2} dx dy = 0.38$ .

tracker based coordinate system utilizing a pinhole model. A star tracker pinhole model is sketched in Fig. 5. A straight line is extended through the equivalent pinhole and the star image on the focal plane. The distance from the equivalent pinhole to the focal plane is the focal length of the lens system. The boresight of the star tracker can be defined as a line passing the geometric center of the focal plane and the equivalent pinhole of the lens system.

In order for the star tracker attitude to be useful, the star tracker internal coordinate system must be known relative to an external reference. The vendor will supply a rotation from the internal coordinate system to an external alignment cube<sup>4</sup> or similar alignment surfaces. This rotation is determined using real sky observations and simultaneous measurements of the alignment cube or a test setup with artificial star stimulation and simultaneous readings on the alignment cube.

In a simple pinhole model, the equations for transforming the centroid coordinates on the focal plane into unit vectors in a star tracker based coordinate system are

$$\begin{pmatrix} i \\ j \\ k \end{pmatrix} = \begin{pmatrix} \cos(\text{atan}2(x - x_0, y - y_0)) \cdot \cos\left(\frac{\pi}{2} - \text{atan}\left(\sqrt{\left(\frac{x - x_0}{F}\right)^2 + \left(\frac{y - y_0}{F}\right)^2}\right)\right) \\ \sin(\text{atan}2(x - x_0, y - y_0)) \cdot \cos\left(\frac{\pi}{2} - \text{atan}\left(\sqrt{\left(\frac{x - x_0}{F}\right)^2 + \left(\frac{y - y_0}{F}\right)^2}\right)\right) \\ \sin\left(\frac{\pi}{2} - \text{atan}\left(\sqrt{\left(\frac{x - x_0}{F}\right)^2 + \left(\frac{y - y_0}{F}\right)^2}\right)\right) \end{pmatrix} \quad (1)$$

where  $(x, y)$  is the focal plane coordinate,  $(x_0, y_0)$  is the intersection of the focal plane and the optical axis,  $F$  is the focal length of the optical system, and  $\text{atan}2$  is four quadrant inverse tangent.

The unit vectors of the stars in an inertial based coordinate system (e.g. J2000) are also known from the firmware star catalog. The average rotation (quaternion or direction cosine matrix) from the inertial based coordinate system to the star tracker based coordinate system can therefore be calculated. Typically the Quest algorithm is used for this [34].

### III. STAR LIGHT SENSITIVITY, DETECTION THRESHOLD, AVERAGE NUMBER OF STARS IN THE FOV AND SKY COVERAGE

The average number of stars in the FOV and the brightness of the stars are very important to the accuracy and the percentage of the sky where the star

<sup>4</sup>An alignment cube is a small, high precision cube with reflecting surfaces mounted on the star tracker. Using an autocollimator it is possible to establish a coordinate system referring to this cube and the star tracker.

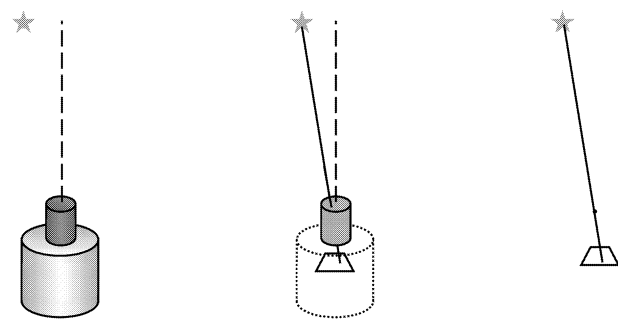


Fig. 5. Sketch of a pinhole star tracker. The dashed line is the boresight of the star tracker. The left sketch shows the star tracker. The center sketch shows x-ray image of the star tracker. In this sketch, focal plane is visible. In the right sketch, the lens system is replaced with equivalent pinhole.

tracker operates. Therefore, this section calculates star light sensitivity and shows how to determine the star detection threshold. Also, equations to calculate the average number of stars in the FOV are shown. Finally, simulations of the percentage of the sky where the star tracker will operate are performed.

Many bright stars in the sky have surface temperatures close to that of the Sun. Therefore, sensitivity to stars of spectral class G2 are calculated in this section. The calculation can easily be done for stellar surface temperatures other than 5800K. The Sun has an apparent magnitude  $M_V = -26.7$  and the solar flux is  $1.3 \text{ KW/m}^2$ . Therefore the Sun is  $2.5^{26.7} = 4.2 \cdot 10^{10}$  times brighter than a magnitude 0 star. The incident energy from an  $M_V = 0$  star on an area of  $1 \text{ mm}^2$  has the same relative spectral characteristic as a black body radiator and the total power is  $(1.3 \text{ KW/m}^2 \times 10^{-6} \text{ m}^2)/4.2 \cdot 10^{10} = 2.96 \cdot 10^{-14} \text{ W}$ .

The radiation from a black body at a given wavelength and temperature is given by [35]

$$I(\lambda, T) = \frac{2 \cdot \pi \cdot h \cdot c^2}{\lambda^5 \cdot (e^{h \cdot c / \lambda \cdot k_B \cdot T} - 1)} \quad (2)$$

where  $h = 6.626 \cdot 10^{-34} \text{ J} \cdot \text{s}$ ,  $c$  is the speed of light =  $2.997 \cdot 10^8 \text{ m/s}$ , and  $k_B$  is Boltzmanns constant =  $1.38 \cdot 10^{-23} \text{ J/K}$ .  $\lambda$  is the wavelength in m and  $T$  is the temperature (in Kelvin).

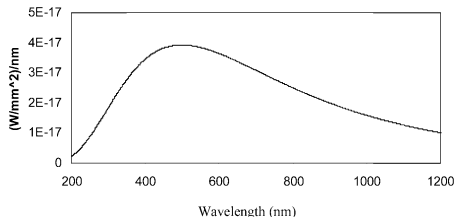


Fig. 6. The power influx from a 5800K,  $M_V = 0$  star on an area of  $1 \text{ mm}^2$ .

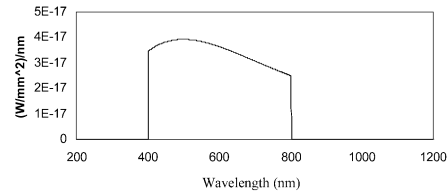


Fig. 7. The power influx from a star on the focal plane.

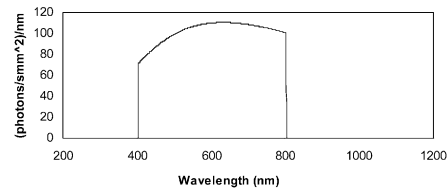


Fig. 8. The photon influx from a star on the focal plane.

The absolute spectral characteristics of the influx from an  $M_V = 0$  star on an area on  $1 \text{ mm}^2$  is found by multiplying a constant to (2) so the total power is  $2.96 \cdot 10^{-14} \text{ W/mm}^2$ . The spectral influx is shown in Fig. 6.

Typically, star tracker optics are coated to minimize reflections, chromatic distortion, and restrict the wavelengths that reach the focal plane because red light diffuse inside the focal plane [36]. In this calculation, it is assumed that the optical system transmits wavelengths in the 400–800 nm band. The resulting power influx on the focal plane is shown in Fig. 7.

The energy of a photon is [35]

$$E = \frac{hc}{\lambda} \quad (3)$$

where  $E$  is the energy in Joules,  $\lambda$  is the wavelength in m,  $h = 6.626 \cdot 10^{-34} \text{ J} \cdot \text{s}$ , and  $c$  is the speed of light =  $2.997 \cdot 10^8 \text{ m/s}$ . It is possible to express the power influx in terms of photons/s by dividing the power influx by the photon energy. The result is shown in Fig. 8.

The fraction of photons that are converted into photoelectrons on the focal plane is called the absolute quantum efficiency (QE) [36]. In Fig. 9 is shown the QE for a typical focal plane array (Kodak KAF-401) [37]. The QE is multiplied with the photon influx. The result is shown in Fig. 10.

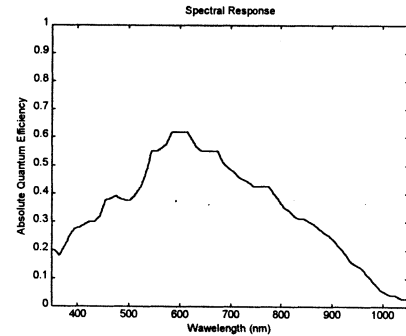


Fig. 9. The QE for a typical silicon focal plane array.

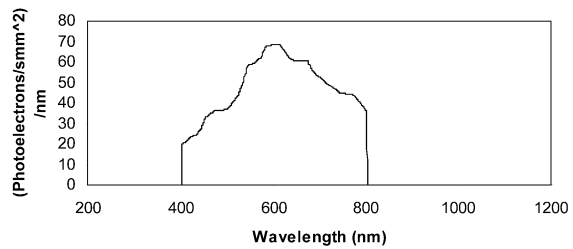


Fig. 10. The detected photons from a star.

The result of summing over the wavelengths in Fig. 10 is 19100 photoelectrons. This means that a star tracker that has an exposure time of 1 s and a lens aperture area on  $1 \text{ mm}^2$  will generate 19100 photoelectrons for a magnitude 0 star of spectral class G2. The number is similar to experimental data [19], [38]. As an example, a star tracker has a 3 cm lens aperture and a 200 ms exposure time. The star tracker images an  $M_V = 4$  star. This star tracker generates

$$19100 \frac{\text{photoelectrons}}{\text{s} \cdot \text{mm}^2} \cdot \frac{1}{2.5^{4-0}} \cdot 0.2 \frac{\text{s}}{\text{exposure}} \cdot \pi \cdot 15 \text{ mm}^2 = 69235 \frac{\text{photoelectrons}}{\text{exposure}}. \quad (4)$$

The star detection threshold is also important and is therefore discussed. The principal contributors to the background signal noise are typically: read noise, inhomogeneity of the dark current, and the dark current noise itself. It is possible to estimate the background noise as the standard deviation of all pixel values in a dark frame. A focal plane consists of up to  $10^6$  pixels and it is therefore reasonable to set the detection threshold for a star signal to be the average background pixel value +5 times the standard deviation to avoid false positives. A star is detected if the brightest pixel in the star is above the threshold.<sup>5</sup> The brightest pixel of a star depends on the point spread function (PSF) and the position of the star. If the star image has a Gaussian PSF radius of 0.5 pixels

<sup>5</sup>It is assumed that stars are detected by sifting the image for pixels above the threshold value. It is possible to improve the detection threshold by sifting the image with a 2 by 2 pixel window or to subtract an “average” background image. However, these approaches require additional processor and memory resources.

and it is centered on a pixel, 29.4%<sup>6</sup> of the signal will be contained in the brightest pixel. However, if the radius of the Gaussian PSF is 1 pixel and the star is centered on the boundary between 4 pixels then the brightest pixel will only contain 12.7%<sup>7</sup> of the signal. The detection threshold for stars is therefore:

$$\text{detection limit} = A_{\text{pixel}} + 5 \cdot \sigma_{\text{pixel}} \cdot \frac{1}{\int_0^1 \int_0^1 \frac{1}{2 \cdot \pi \cdot \sigma_{\text{PSF}}} e^{-x^2+y^2/2 \cdot \sigma_{\text{PSF}}} dx dy} \quad (5)$$

where  $A_{\text{pixel}}$  is the mean value of the pixels,  $\sigma_{\text{pixel}}$  is the standard deviation of the pixel values in a dark frame, and  $\sigma_{\text{PSF}}$  is the PSF radius in pixels (assuming a Gaussian PSF).

The average number of stars in the FOV is also essential to the accuracy and sky coverage of a star tracker. It is assumed that the FOV is circular and is A deg wide. The fraction of the sky that is covered by the FOV is then:

$$\frac{1 - \cos\left(\frac{A}{2}\right)}{2}. \quad (6)$$

The number of stars brighter than a given magnitude can be estimated by plotting the number of stars brighter than a given magnitude versus magnitude. This was done for the PPM star catalog in an Excel spreadsheet. The relationship was found to be

$$N = 6.57 \cdot e^{1.08 \cdot M} \quad (7)$$

where  $N$  is the total number of stars on the sky and  $M$  is the visual magnitude ( $M_V$ ).

The average number of stars in the FOV is then:

$$N_{\text{FOV}} = 6.57 \cdot e^{1.08 \cdot M} \cdot \frac{1 - \cos\left(\frac{A}{2}\right)}{2}. \quad (8)$$

As an example, a star tracker has a detection threshold of  $M_V = 5$ . The star tracker FOV is  $15^\circ$ . On average, the star tracker will detect 6.2 stars in the FOV.

Sky coverage is defined as the percentage of the sky where the star tracker will operate. Ideally a star tracker should be able to operate at all attitudes, but two stars must, as a minimum be present in the FOV to calculate the attitude solution. The stars are not distributed homogeneously on the sky—there are many stars in the galactic plane and relatively fewer at the galactic poles. Therefore, there are areas on the sky, where there are not enough stars for some star trackers to operate.

Fig. 11 show a simulation of the percentage of sky where there are more than one star in the FOV as a function of the FOV size for different detection

<sup>6</sup>  $\int_{-0.5}^{0.5} \int_{-0.5}^{0.5} (1/2 \cdot \pi \cdot 0.5) e^{1x^2+y^2/2-0.5} dx dy$ .  
<sup>7</sup>  $\int_0^1 \int_0^1 (1/2 \cdot \pi \cdot 1) e^{1x^2+y^2/2-1} dx dy$ .

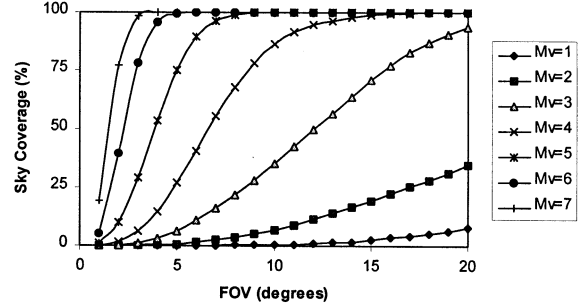


Fig. 11. The theoretical sky coverage as a function of FOV and detection threshold.

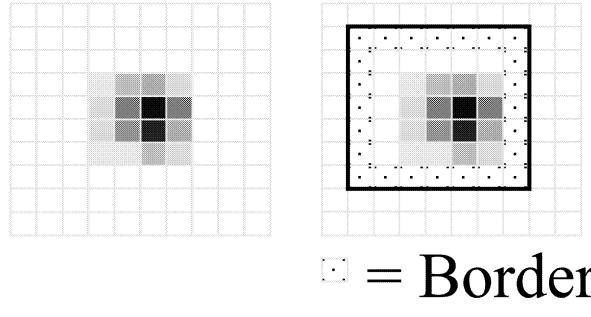


Fig. 12. ROI and the border of ROI of detected star.

thresholds. As an example, a star tracker with a FOV on  $10^\circ$  and a detection threshold on  $M_V = 4$  will only have more than 1 star in the FOV in 87% of the time. The theoretical sky coverage is therefore 87%. It should be noted that this is the theoretical limit. Normally, a star tracker requires more than 2 stars in the FOV to operate, depending on the implementation. The initial attitude acquisition will typically require much more stars. Most star trackers are designed to have sky coverage close to 100%.

#### IV. STAR CENTROIDING

Star trackers utilize subpixel centroiding to increase the accuracy. In a focused image a star appears as a point source, so all the photoelectrons from a star are generated in a single pixel. However, if the optics is slightly defocused a star will occupy several pixels. This facilitates calculating the center of the star with subpixel accuracy. This section discusses an algorithm for calculating centroids and making centroiding accuracy simulations.

Initially, the image is sifted for pixels that are above a given threshold. Once a pixel is detected, a region of interest (ROI) window is aligned with the detected pixel in the center. The average pixel value on the border is calculated and subtracted from all pixels in the ROI as shown in Fig. 12. The centroid ( $(x_{cm}, y_{cm})$ ) and  $DN$  (brightness) are calculated from the background-subtracted pixels in the ROI.

$$DN = \sum_{x=\text{ROIstart}+1}^{\text{ROIend}-1} \sum_{y=\text{ROIstart}+1}^{\text{ROIend}-1} \text{image}(x, y) \quad (9)$$

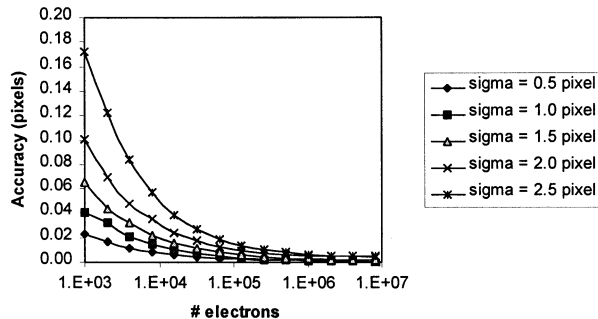


Fig. 13. The simulation of the centroiding accuracy as function of the number of photoelectrons.

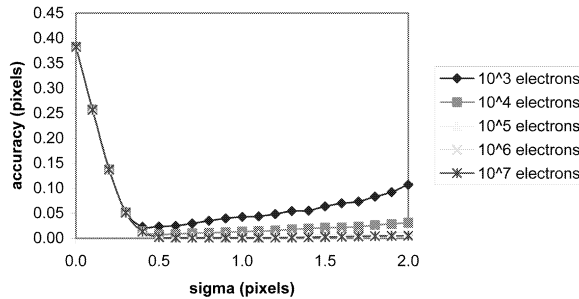


Fig. 14. Simulation of the centroiding accuracy as a function of the size of the PSF.

$$x_{cm} = \sum_{x=ROIstart+1}^{ROIend-1} \sum_{y=ROIstart+1}^{ROIend-1} \frac{x \cdot \text{image}(x,y)}{DN} \quad (10)$$

$$y_{cm} = \sum_{x=ROIstart+1}^{ROIend-1} \sum_{y=ROIstart+1}^{ROIend-1} \frac{y \cdot \text{image}(x,y)}{DN}. \quad (11)$$

The centroiding accuracy is proportional to the square root of the number of photoelectrons generated by the star. In Fig. 13 is shown the centroiding accuracy as a function of the number of detected photoelectrons for various sizes of the PSF radius. In the simulation, the only noise source is the photon noise. A Gaussian PSF, 100% QE, and a  $9 \times 9$  pixel ROI have been assumed.

In Fig. 14 the centroiding accuracy is shown as a function of the size of the PSF radius for stars with different number of photoelectrons. In the simulation only photon noise is included, a QE on 100%, a Gaussian PSF, and an ROI on  $9 \times 9$  pixels are assumed. It is observed that the centroiding accuracy does not have a strong dependence on the size of the PSF radius as long as it has a radius of more than 0.5 pixels. The reason for this is that the accuracy is limited by the sampling theorem when the PSF radius is less than 0.5 pixels. In real implementations it is also important to have a small ROI because of pixel inhomogeneity and noise, that is not included in this simulation. However, it must be ensured that the star signal does not fall outside the ROI.

In Fig. 15 is shown a simulation of the centroiding accuracy as a function of the noise level. As an

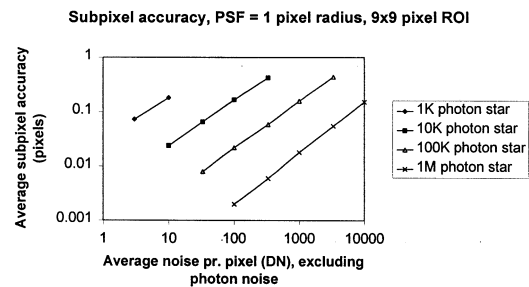


Fig. 15. Simulation of the centroiding accuracy.

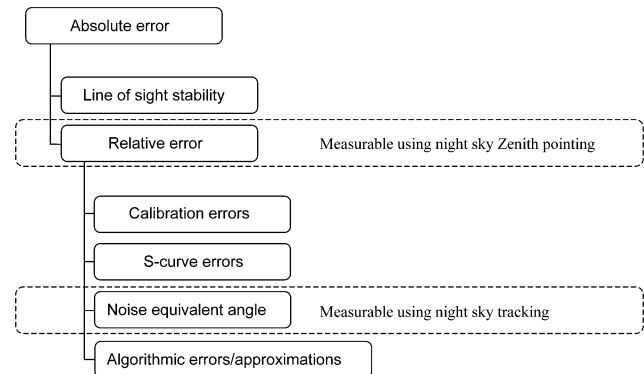


Fig. 16. Typical error tree for a star tracker.

example, a star is known to have a read/dark current noise on 100 photoelectrons. The brightness of the star is 100000 photoelectrons. The average centroiding accuracy will then be  $\sim 0.2$  pixels. In this simulation a QE on 100%, a Gaussian PSF, and a  $9 \times 9$  pixel ROI are assumed.

The simulations shown in Figs. 13–15 generated a Gaussian shaped star and added photon noise to it. The centroid was then calculated. This scenario was repeated a large number of times to calculate the statistical average accuracy.

## V. STAR TRACKER ACCURACY

This section discusses the attitude accuracy of a star tracker. Attitude accuracy is typically divided into different categories. These categories are discussed and simple empirical rules for estimating some of them are shown.

The attitude output of an autonomous star tracker can be a direction cosine matrix, a quaternion or three Euler angles [39]. Typically a coordinate system is defined on the star tracker itself with one axis aligned with the boresight of the star tracker. This axis is typically called the roll or twist axis. The other two axes are traditionally called the yaw and pitch or cross boresight axes. Vendors typically quote the rms accuracy of a star tracker in one cross boresight axis. In Fig. 16, the errors in a star tracker are specified in an error tree. It is possible to make more elaborate representations [24].

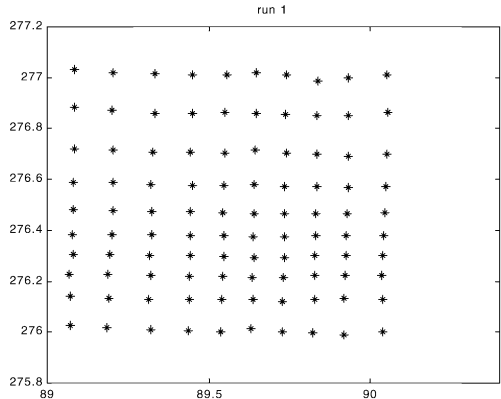


Fig. 17. Equally spaced grid on  $10 \times 10$  grid points, acquired within the same pixel of a star tracker.

**Absolute Error:** The absolute attitude error of a star tracker is defined as the attitude differences between the alignment cube attitude of the star tracker and the measured attitude. It consists of two categories, the line of sight uncertainty and the relative error.

**Line of Sight Uncertainty:** The line of sight uncertainty consists primarily of small mechanical excursions in the star tracker, which cannot be calibrated out. These excursions are caused by thermal expansions, launch effects, etc.

**Relative Error:** This error represents the star tracker's ability to measure angular distance between two attitudes. The relative error consists of four different categories: calibration errors, S-curve errors, NEA, and algorithmic errors/approximations. This accuracy can be measured directly using night sky observations. This is discussed further in Section VI.

**Calibration Errors:** This is the error caused by not having an ideal model and calibration of the camera/optics. This includes inaccurate focal length estimate, inaccurate intersection/angle of boresight, and focal plane. Also, uncalibrated optical distortion and chroma/astigmatism is included in this category. The calibration of a star tracker is discussed further in Section VII.

**S-curve Error:** In this category, all pixel periodic errors of the centroiding algorithm are assembled. The centroiding errors were discussed in Section IV and depend on the homogeneity of the pixel response, dark current, PSF, full well, brightness, and charge transfer efficiency. If the focal plane array has been subjected to radiation, this error tends to get worse because the sensitivity/dark-current gets more nonuniform and the dark current increases.

An average pixel periodic correction can be constructed. However, it typically changes slowly over the FOV. As an example, Fig. 17 shows a star that has been moved in an equally spaced grid of  $10 \times 10$  points within the same pixel on a star tracker. An equally spaced grid was expected, but the grid is not equally spaced due to S-curve errors primarily caused

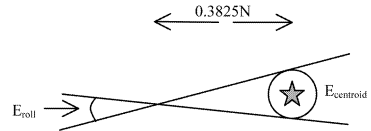


Fig. 18. The roll uncertainty of a star.

by an asymmetrical PSF. It is possible to calculate a correction that will map the nonequally spaced grid into an equally spaced grid. This is called an S-curve correction [38].

**Noise Equivalent Angle:** The NEA is the star tracker's ability to reproduce the same attitude provided the same optical stimulation. This error exclusively reflects the hardware (it is independent of software, algorithms, and calibration). It consists of photon noise, dark current noise, read/amplifier noise, limited resolution of the analog-to-digital (A/D) converter, and random error on the timestamp of the attitude estimate.

It is possible to estimate the NEA of a star tracker based on a few star tracker parameters. The cross boresight NEA (one axis) is approximately

$$E_{\text{cross-boresight}} = \frac{A \cdot E_{\text{centroid}}}{N_{\text{pixel}} \cdot \sqrt{N_{\text{star}}}} \quad (12)$$

where  $A$  is the FOV of the star tracker, typically ranging from  $1^\circ$  to  $40^\circ$ .  $E_{\text{centroid}}$  is the average centroiding accuracy, typically ranging from 0.01 to 0.5.  $N_{\text{pixels}}$  is the number of pixels across the focal plane, typically ranging from 256–1024.  $N_{\text{stars}}$  is the average number of detected stars in the camera image, typically 3–200. As an example, a star tracker has a focal plane of  $512 \times 512$  pixels and a FOV of  $15^\circ$ . The star centroid noise is 1/10 of a pixel and there are on the average 20 stars in the FOV. The NEA of the star tracker is then approximately

$$\frac{15^\circ \cdot 0.1 \text{ pixel}}{512 \text{ pixels} \cdot \sqrt{20 \text{ stars}}} = 2.3 \text{ arcseconds.} \quad (13)$$

The roll NEA of a star tracker is less accurate than the boresight accuracy. The reason for this is that the dimension of the focal length is larger than the focal plane itself. A typical star tracker is 6–16 times less accurate in the roll axis. The following approximation can be used to estimate the roll accuracy of a star tracker. A quadratic  $N \times N$  pixel focal plane is assumed. The average distance from a star to the center of the focal plane is

$$\int_{-N/2}^{N/2} \int_{-N/2}^{N/2} \sqrt{x^2 + y^2} dx dy = 0.3825N. \quad (14)$$

The average star has a spatial uncertainty on  $E_{\text{centroid}}$ . This is transformed into roll accuracy,  $E_{\text{roll}}$ , as shown in Fig. 18.

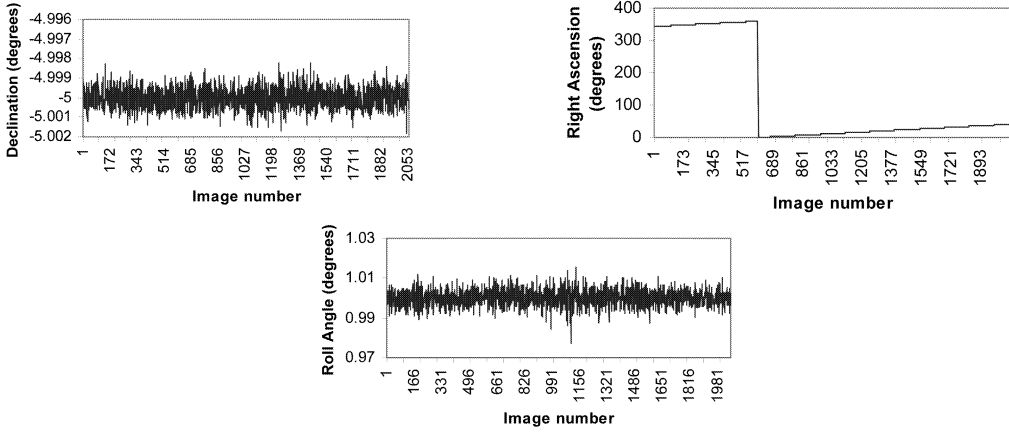


Fig. 19. Typical attitude output from a Zenith pointing series.

In Fig. 18 it is observed that the uncertainty on the roll axis from an average star is

$$E_{\text{roll, single star}} = \text{atan} \frac{E_{\text{centroid}}}{0.3825 \cdot N_{\text{pixel}}}. \quad (15)$$

Therefore, the roll accuracy for the entire attitude estimate is

$$E_{\text{roll}} = \text{atan} \left( \frac{E_{\text{centroid}}}{0.3825 \cdot N_{\text{pixel}}} \right) \cdot \frac{1}{\sqrt{N_{\text{stars}}}}. \quad (16)$$

As an example, the roll accuracy of the star tracker from the previous example will approximately be

$$\text{atan} \left( \frac{0.1 \text{ pixel}}{0.3825 \cdot 512 \text{ pixels}} \right) \cdot \frac{1}{\sqrt{20}} = 23 \text{ arcseconds}. \quad (17)$$

Some algorithms only utilize stars within a given distance from the center of the FOV [40]. This will tend to reduce the roll accuracy. Note that the roll accuracy does not depend on the FOV but only on the number of pixels and the centroiding accuracy.

*Algorithmic Error Approximations:* These are the errors that are due to approximations/limited accuracy in the algorithms. False stars<sup>8</sup> might also be confused to be a star, perturbing the attitude estimate. Also inaccuracies in the firmware star catalog are included in this category. Section VIII discusses this issue further.

## VI. MEASURING STAR TRACKER ACCURACY

One method to estimate the relative accuracy of a star tracker is to perform actual night sky observations. For this type of measurement, it is advantageous to transform the attitude output of the star tracker into celestial coordinates [39]. A high quality telescope drive must be utilized so drift

and noise from the telescope drive is minimized. The telescope drive is pointed towards the zenith. The declination and roll angle will remain constant whereas the right ascension will drift at the sidereal rate.<sup>9</sup> It is possible to estimate the relative accuracy of a star tracker as the statistical fluctuations of the declination and roll angle or the right ascension when the sidereal rate has been subtracted. In Fig. 19 are shown a simulation of the attitude components of a zenith pointing series. The statistical fluctuation of the declination in this simulation is 1.8 arcseconds (rms). The statistical fluctuation of the roll component in this simulation is 14 arcseconds (rms). It is observed that the right ascension drifts with the sidereal rate. The big attitude jump is an artifact of the angle jumping from 360° to 0°.

All ground based observations include atmospheric seeing<sup>10</sup> which changes the shape of the star images. The effect typically causes a random error in the 1 arcsecond range. Star observations also include atmospheric refraction. Refraction causes a star to appear to be closer to zenith than it is due to the atmosphere. The refraction is a function of the zenith distance. As an example, the position of a star viewed at the horizon will be shifted approximately 34 arcminutes towards zenith [43]. When testing a star tracker on Earth, the star tracker should compensate for refraction.

Note that the right ascension is shortened with the cosine of the declination. This means that it appears as the accuracy of a star tracker decreases as it is points towards the poles. The roll accuracy near the poles is

<sup>9</sup>This is not completely true. Various small effects such as nutation, aberration, etc., have to be included if the tests are conducted over long time [41].

<sup>10</sup>Seeing is the result of variations in the index of refraction of the air over size scales smaller than the aperture. These variations introduce random phase delays in the incoming electromagnetic waves, which have the same effect as irregularities in the shape of the aperture [42].

<sup>8</sup>A proton or a heavy ion impinging on a focal plane will cause a bright spot that can be perceived as a star.

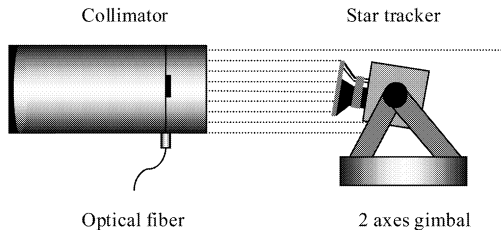


Fig. 20. Laboratory setup to characterize a star tracker.

also coupled to the right ascension and appears to be less accurate. However, these effects are just artifacts of how the angles are defined.

It is also possible to estimate the accuracy of a star tracker utilizing a laboratory setup as sketched in Fig. 20. A collimated light source is placed in front of the star tracker. The star tracker is mounted on a 2 axes precision gimbal [44]. The collimated light source will be perceived as a single star that is moving around in the FOV when the gimbals rotate. Arcsecond accuracy levels can be achieved with this kind of setup.

The NEA can also be estimated utilizing night sky observations. Commanding the telescope drive to track a specific part of the sky (near zenith, to minimize atmospheric perturbations) does this. An equatorial mount is compensating for the Earth motion so the attitude will remain constant. Depending on the telescope drive, it may be compensating for various small effects such as precession, nutation, aberration, etc. It is possible to estimate the NEA as the statistical fluctuations of the attitude angles. Fig. 21 shows the attitude components from a tracking series simulation. The statistical fluctuation of the declination and right ascension is 1.2 arcseconds rms. The statistical fluctuation of the roll angle is 9 arcseconds (rms).

Finally, an autonomous star tracker can also be mounted in a scene simulation setup. A CRT or TFT monitor is placed in front of the star tracker and a collimating lens is placed in front of the star tracker

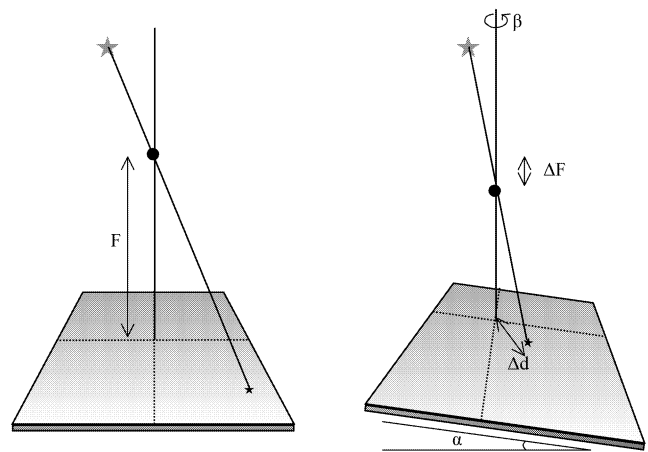


Fig. 22. (a) Star tracker pinhole model. (b) Real world star tracker model.

optics. The monitor then displays simulated images of the sky. This setup can test functionality, initial attitude acquisition, etc. [45]. However, this kind of setup is not accurate enough to estimate the accuracy of a star tracker.

## VII. STAR TRACKER CALIBRATION

The positions of the star centroids on the focal plane were transformed into unit vectors in a star tracker based coordinate system utilizing a pinhole model (equation 1). In the pinhole model, various physical parameters must be estimated (e.g. the focal length of the lens system). The estimation of these parameters is called the star tracker calibration. A simple pinhole star tracker model is shown in Fig. 22(a). The star tracker pinhole model may have various complexities. It may include tilt of the focal plane, focal length, intersection of boresight and the focal plane, optical distortion correction polynomial, correction polynomial for star surface temperature, etc.

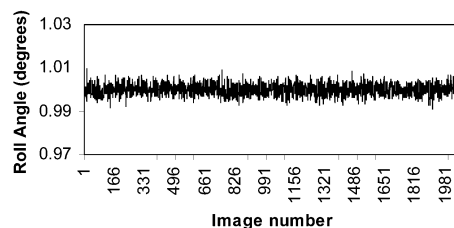
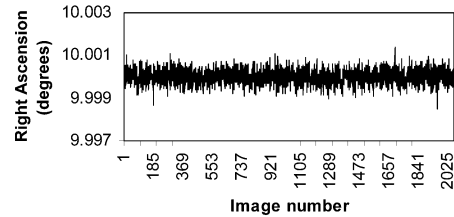
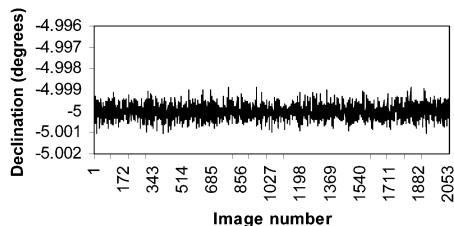


Fig. 21. Typical attitude output from a tracking series.

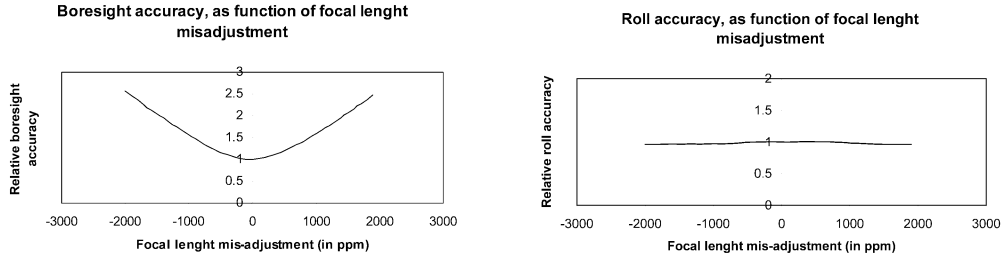


Fig. 23. The relative accuracy as a function of the focal length estimate.

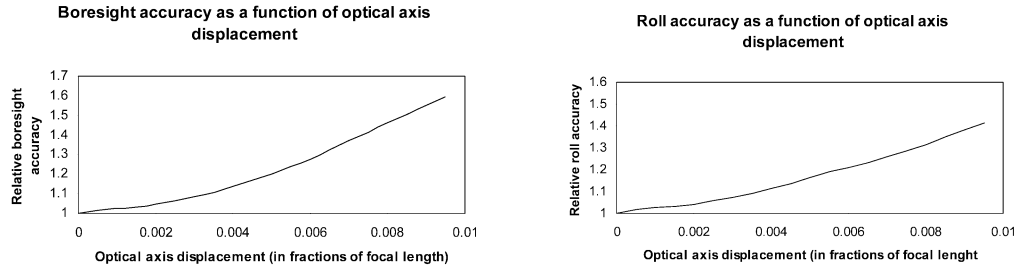


Fig. 24. The relative accuracy as a function of the intersection of the optical axis and the focal plane estimate.

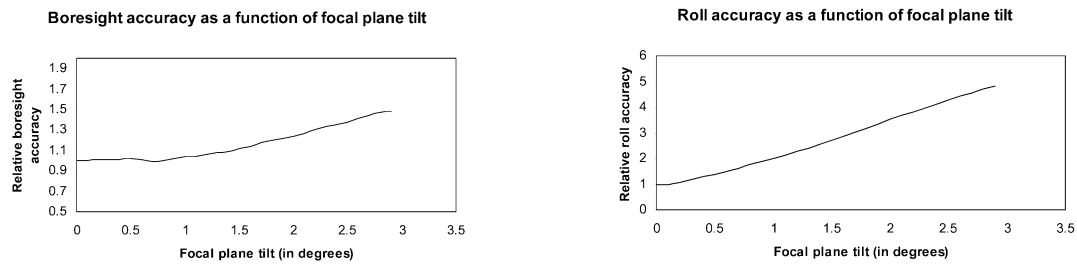


Fig. 25. The relative accuracy as a function of the angle between the optical axis and the focal plane estimate.

There are always small differences between the actual and the estimated parameters of a model. This is the calibration error. In Fig. 22(b), the following differences are identified.  $\Delta F$  error in focal length,  $\Delta d$  displacement of intersection of optical axis and focal plane array.  $\alpha$  is the angle that the focal plane is not orthogonal to the optical axis.  $\beta$  is the rotational error of the focal plane. Additionally, a number of imperfections exist such as optical distortion, etc.

To investigate how sensitive the accuracy of the star tracker is to adjustments of the model parameters a number of simulations have been made. In each simulation a parameter has been changed a percentage and the resulting star tracker accuracy (relative to the accuracy with the optimal parameters) has been calculated. The results of the simulations are shown in Figs. 23–25. The precise dependencies will vary for different star tracker implementations but the simulation shows the general trends.

Fig. 23 shows that the boresight accuracy of a star tracker is extremely sensitive to inaccuracies in the focal length estimate. Typically the focal length must be known to within microns not to degrade the boresight accuracy. Fig. 23 also shows that the roll accuracy is almost independent of how well the

focal length is estimated. Both the boresight accuracy and the roll accuracy are somewhat sensitive to the estimate of the intersection of the focal plane and the optical axis. Fig. 24 shows that the estimates may be several pixels off without any significant degradation of the accuracy. Finally, in Fig. 25 the simulations show that estimates of the focal plane angle to the optical axis do not affect the boresight accuracy significantly, but the roll accuracy is very sensitive to inaccuracies.

There might be small changes in the lens system during launch. Therefore small corrections to the model parameters are sometimes performed after launch. This “in-flight” calibration can increase the accuracy of a star tracker.

## VIII. FIRMWARE STAR CATALOG

An autonomous star tracker has an internal star catalog in the firmware. This star catalog is used for the initial attitude acquisition and for calculating the attitude quaternion. Inaccuracies in the internal star catalog generate attitude errors. This section discusses the compilation of the internal star catalog and shows simulations of how

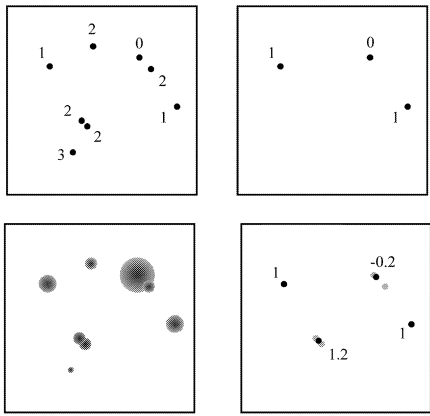


Fig. 26. Compiling the internal star catalog.

inaccuracies in the star catalog affect the attitude output.

A number of star catalogs are available from web-site sites [46, 47]. The most recent catalog is the HIPPARCOS star catalog [48]. The compilation of the internal star tracker catalog is a delicate process. Initially, the brightness of the stars has to be transformed into brightness corresponding to the spectral sensitivity of the star tracker. Secondly, the star tracker optics is defocused. This means that close stars are merging and appearing as a single star with a new position. This phenomenon is sketched in Fig. 26. In the upper left sketch, an (artificial) part of the sky is shown. In this example it is assumed that the detection threshold is magnitude 1.5. A simple selection process would result in an internal star catalog shown in the upper right sketch. However, the star tracker image is defocused and will perceive the sky as shown in the lower left sketch. Two pairs of stars are merged and the brightness is added. The compiled star tracker catalog should be as shown in the lower right sketch. The gray dots in the lower right sketch are the original star positions for reference. An alternative is to flag all stars with the potential of merging with dimmer stars and reject them in the attitude calculation.

Inaccuracies in the internal star tracker catalog will cause errors on the attitude output. To illustrate this a simulation has been performed. In the simulation a star catalog error on 52 arcseconds is introduced on a single star and the simulation from Fig. 19 is repeated. The star with the artificial error enters approximately

1/3 into the series and exists approximately 2/3 into the series. The result of the simulation is shown in Fig. 27. The accuracy of this simulation is 2.8 arcseconds (rms) cross boresight and 22 arcseconds (rms) in roll. Different algorithms will respond differently to star catalog errors, however this simulation shows the general trend of a star catalog error.

## IX. SUMMARY

This paper has discussed different aspects of autonomous star trackers. Initially, it was explained how an autonomous star tracker operates. Various radiometric calculations were performed to assess the sensitivity of a star tracker, the detection threshold for stars, the average number of stars in the FOV, and the sky coverage. Algorithms for star centroiding were discussed and the performance was simulated. An error tree typically represents the accuracy of a star tracker. The most important categories are the relative accuracy and the NEA. These accuracies can be measured directly utilizing a telescope drive and night sky observation. The calibration of a star tracker was also discussed and simulations were presented. Finally, the compilation of the internal star catalog was discussed.

## REFERENCES

- [1] Liebe, C. C., Jørgensen, J. L. (1996) Algorithms onboard the Oersted micro satellite stellar compass. *SPIE Proceedings*, **2810**, Denver (1996), 239–251.
- [2] Officine Galileo, Italy: Thomas, V. C., et al. (1994) Cassini star tracking and identification architecture. *SPIE Proceedings*, **2221** (1994), 15–26.
- [3] Ball Aerospace, USA (2001) URL: <http://www.ball.com/aerospace/senst.html>. (Cited Jan. 4, 2001.)
- [4] EMS Technologies, Canada (2001) URL: <http://www.calcorp.com/ssgopt.htm>. (Cited Jan. 4, 2001.)
- [5] Jena Optronik, Germany (1990) Astro 1M, Jenauer Rundschau, 1/1990.
- [6] Technical University of Denmark, Denmark: Jørgensen, J. L., and Liebe, C. C. (1996) The advanced stellar compass, development and operations. *Acta Astronautica*, **39**, 9–12 (1996), 775–783.

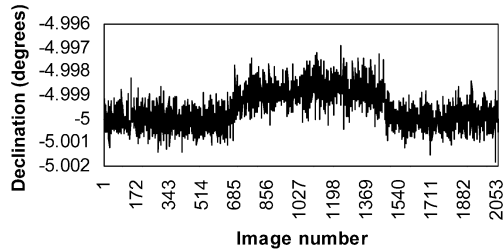
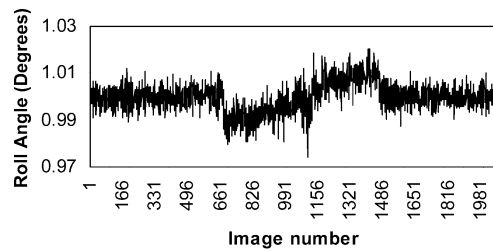
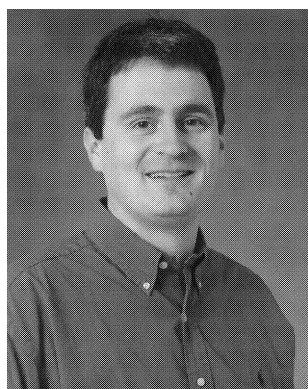


Fig. 27. Simulation showing how inaccuracies in the internal star catalog will affect the attitude estimate.



- [7] Space Research Institute of the Russian Academy of Sciences, Russia (1999)  
URL: [http://wildecat.iki.rssi.ru/ASTRO\\_star\\_E.htm](http://wildecat.iki.rssi.ru/ASTRO_star_E.htm). (Cited Jan. 1999.)
- [8] Kayser Threde, Germany (2001)  
URL:  
[http://www.kayser-threde.de/news/starsensor\\_0998e.htm](http://www.kayser-threde.de/news/starsensor_0998e.htm). (Cited Jan. 4, 2001.)
- [9] Lockheed Martin, USA: von Bezooijen, R. W. H. (1994) True sky demonstration of an autonomous star tracker. *SPIE*, **2221** (1994), 156–169.
- [10] Corning OCA, USA (1999)  
URL: [http://www.oca.com/ao\\_eosens.htm](http://www.oca.com/ao_eosens.htm). (Cited Jan. 1999.)
- [11] Cassidy, L.W. (1996) Space qualification of HDOS' HD-1003 star tracker, space sciencecraft control and tracking in the new millennium.  
In *Proceedings of the SPIE Conference*, Denver, CO, Aug. 6–8, 1996; *SPIE Proceedings*, **2810** (1996), 213–220.
- [12] SIRA electro-optics, England (2001)  
URL: <http://www.siraeo.co.uk/default.asp?fid=0,2,12>. (Cited Jan. 4, 2001.)
- [13] Sodern, France: Pissavini, P., et al. (1997) Improved star tracker for Odin satellite.  
Presented at the ESA International Conference on Spacecraft Guidance, Navigation and Control Systems, 3rd, Noordwijk, Netherlands, Nov. 26–29, 1996; In *Proceedings* (A97-4050111-18), Noordwijk, Netherlands, ESA, 1997, 611–616.
- [14] Space Innovations Limited, England (1999)  
URL: <http://www.sil.com/subsys/sensors/starmapp.htm>. (Cited Jan. 1999.)
- [15] Surrey Satellite Technology Ltd., England (1999)  
URL:  
[http://www.sstl.co.uk/services/subpage\\_services.html](http://www.sstl.co.uk/services/subpage_services.html). (Cited Jan. 1999.)
- [16] TERMA, Denmark: Paulsen, T. E., et al. (2000) Calibration and verification of the TERMA star tracker for the NEMO satellite.  
Presented at the AIAA Space 2000 Conference and Exposition, Long Beach, CA, Sept. 19–21, 2000.
- [17] Carbone, J., et al. (1995) New CID detectors/cameras for use in ionizing radiation environments.  
In *Proceedings of 43rd Conference on Robotics and Remote Systems*, 1995, 43–50.
- [18] Kaufman, B., et al. (1993) Field test results for a CID star tracker.  
In *Proceedings of the Annual Rocky Mountain Guidance and Control Conference*, Keystone, CO, Feb. 6–10, 1993 (A94-24492 06-63); San Diego, CA, Univelt, Inc., 1993, 389–408.
- [19] Liebe, C. C., Dennison, E. W., Hancock, B., Stirbl, R. C., and Pain, B. (1998) Active pixel sensor (APS) based star tracker.  
In *Proceedings of the IEEE Aerospace Conference*, Aspen, CO, Mar. 21–28, 1998, 119–127.
- [20] Stirbl, R., et al. (1998) Next generation CMOS active pixel sensors for satellite hybrid optical communications/imaging sensor systems sensors, systems, and next-generation satellites II. *SPIE Proceedings*, **3498** (1998), 255–264.
- [21] Zhou, Z. et al. (1997) CMOS active pixel sensor with on-chip successive approximation analog-to-digital converter.  
*IEEE Transactions on Electron Devices*, **44**, 10 (Oct. 1997), 1759–1763.
- [22] Sun, C., et al. (1999) A smart CMOS imager with on-chip high-speed windowed centroiding capability.  
In *Proceedings of 1999 IEEE Workshop on Charge-Coupled Devices and Advanced Image Sensors*, Nagano, Japan, June 10–12, 1999, Paper R9.
- [23] Liebe, C. C. (1995) Star trackers for attitude determination.  
*IEEE AES Magazine*, (June 1995), 10–16.
- [24] Eisenman, A., Liebe, C. C. (1998) The advancing state-of-the-art in second-generation star trackers.  
In *Proceedings of the 1998 IEEE Aerospace Conference*, Aspen, CO, Mar. 21–28, 1998, 111–118.
- [25] van den Heide, E. J., et al. (1998) Development and validation of a fast and reliable star sensor algorithm with reduced data base.  
Presented at the 49th International Astronautical Congress, Melbourne, Australia, Sept. 28–Oct. 2, 1998.
- [26] Liebe, C. C. (1992) Pattern recognition of star constellations for spacecraft applications.  
*IEEE AES Magazine*, (June 1992), 34–41.
- [27] Padgett, C., et al. (1997) Evaluation of star identification techniques.  
*Journal of Guidance Control Dynamics*, **20**, 2 (Mar.–Apr. 1997), 259–267.
- [28] Udomkesmalee, S., et al. (1994) Stochastic star identification.  
*Journal of Guidance Control Dynamics*, **17**, 6 (Nov.–Dec. 1994), 1283–1286.
- [29] Quine, B., et al. (1996) Rapid star pattern identification, acquisition, tracking, and pointing.  
*SPIE Proceedings*, **2739** (1996), 351–360.
- [30] Strikwerda, et al. (1991) Autonomous star identification and spacecraft attitude determination with CCD star trackers.  
In *Proceedings of the First International Conference on Spacecraft Guidance, Navigation and Control Systems*, ESTEC, Noordwijk, The Netherlands, 4–7 June 1991 (ESA, SP-323, Dec. 1991).
- [31] Mortari, D. (1997) Search-less algorithm for star pattern recognition.  
*Journal of Astronaut Sciences*, **45**, 2 (Apr.–Jun. 1997), 179–194.
- [32] Salomon, P. M., Glavich, T. A. (1981) Image processing in sub-pixel accuracy star trackers.  
*SPIE Proceedings*, **290** (1981), 290.
- [33] Stone, R. C. (1989) A comparison of digital centering algorithms.  
*Astronomical Journal*, **97** (Apr. 1989), 1227–1237.
- [34] Shuster, M. D., Oh, S. D. (1981) Three-axis attitude determination from vector observations.  
*Journal of Guidance and Control*, **4**, 1 (Jan.–Feb. 1981), 70–77.
- [35] Serway, R. A., Beichner, R. J. (2000) Physics for scientists and engineers with modern physics. New York: Harcourt, 2000. ISBN: 0030317169.
- [36] Buil, C. (1991) CCD astronomy, construction and use of an astronomical CCD camera.  
Willmann-Bell, 1991. ISBN: 0943396298.
- [37] Kodak (2001) URL: <http://www.kodak.com/US/en/digital/ccd/kaf0401LE.shtml>. (Cited Jan. 4, 2001.)

- [38] Stanton, R. H., et al. (1984) ASTROS: A sub-arcsec CCD star tracker. *SPIE*, **501** (State of the Art Imaging Arrays and Their Application) (1984).
- [39] Wertz, J. R. (1978) *Spacecraft Attitude Determination and Control*. Boston: D. Reidel Publishing Co., 1978.
- [40] Alexander, J. W., and Chang, D. H. (1996) Cassini star tracking and identification algorithms, scene simulation, and testing, Cassini/Huygens: A mission to the Saturnian systems. *SPIE Proceedings*, **2803** (1996), 311–331.
- [41] Seeds, M. A. (1998) *Horizons, Exploring the Universe*. Wadsworth Publishing Co., 1998. ISBN: 0-534-52434-6.
- [42] Seeing (1999) URL: [http://gulliver.gps.caltech.edu/Thesis\\_Chapter\\_2/Introduction.html](http://gulliver.gps.caltech.edu/Thesis_Chapter_2/Introduction.html). (Cited Jan. 1999.)
- [43] Her majesty's Nautical Almanac Office: Royal Greenwich Observatory (1995) The Astronomical Almanac for the Year 1996. HMSO 1995.
- [44] Ball Aerospace (2001) URL: <http://www.ball.com/aerospace/sentest.html>. (Cited Jan. 4, 2001.)
- [45] Gullapalli, S. N, Flynn, D. J, Kiss, F. J, Gauthier, A. G, and Kenney, T. M (1993) ASTRA1 solid state star trackers for Martin Marietta's modular attitude control system module. *SPIE Proceedings*, **1949** (1993), 127–137.
- [46] Simbad, France (2001) URL: <http://cdsweb.u-strasbg.fr/Simbad.html>. (Cited Jan. 4, 2001.)
- [47] Goddard Space Flight Center, NASA (2001) URL: <http://legacy.gsfc.nasa.gov/cgi-bin/W3Browse/w3catindex.pl>. (Cited Jan. 4, 2001.)
- [48] HIPPARCOS homepage (2001) URL: <http://astro.estec.esa.nl/SA-general/Projects/Hipparcos/catalog.html>. (Cited Jan. 4, 2001.)



**Carl Christian Liebe** received the M.S.E.E. degree in 1991 and the Ph.D. degree in 1994 from the Department of Electrophysics, Technical University of Denmark.

Since 1997 he has been with the Jet Propulsion Laboratory, California Institute of Technology. Currently, he is a senior member of the technical staff in the Precision Motion Control Systems & Celestial Sensors Group. He has more than 10 years of experience in star trackers. His current research interests include miniaturization of attitude determination sensors.

Dr. Liebe has authored/co-authored more than 40 papers.